Sound & Vibration 2026, 60(3), 4199.
doi: https://doi.org/10.59400/sv4199

Article

Grouped inerter-resonator arrays for broadband reduction of plate mobility and radiated sound power using modal receptance synthesis

Yogeesh Nijalingappa[1,2,*], Asokan Vasudevan[3], Mustafa Abdullah[4], Shankaralingappa Bheemasandra Marulappa[5], Suleiman Ibrahim Mohammad[2], Ashalatha Kodihalli Siddagangaiah[6]

[1] Department of Mathematics, Government First Grade College, Tumkur 572102, India
[2] Research Fellow, INTI International University, Nilai 71800, Malaysia
[3] Faculty of Business and Communications, INTI International University, Nilai 71800, Malaysia
[4] Hourani Center for Applied Scientific Research, Faculty of Engineering, Al-Ahliyya Amman University, Amman 19111, Jordan
[5] Department of Mathematics, Government First Grade College for Women, Hassan 573201, India
[6] Department of Mathematics, Vedavathi Government First Grade College, Hiriyur 577598, India
* **Corresponding author:** Yogeesh Nijalingappa, yogeesh.r@gmail.com

CITATION

Nijalingappa Y, Vasudevan A, Abdullah M, et al. Grouped inerter-resonator arrays for broadband reduction of plate mobility and radiated sound power using modal receptance synthesis. Sound & Vibration. 2026; 60(3): 4199. https://doi.org/10.59400/sv4199

ARTICLE INFO

Received: 26 March 2026
Revised: 15 April 2026
Accepted: 20 April 2026
Available online: 9 June 2026

Abstract: A plate-type vibroacoustic treatment is developed in which a simply supported Kirchhoff plate is coupled to a grouped array of parallel spring-damper-mass-inerter attachments. The emphasis is intentionally computational. The plate equation is reduced to a modal receptance form using 36 orthogonal sine modes, and the local attachments are eliminated analytically so that each attachment contributes a rank-one dynamic stiffness term. The resulting frequency-domain matrix remains explicit and can therefore be evaluated over large parameter grids without rederiving the governing equations. For the present plate, the bending rigidity is $D = 102.285$ N·m, the areal density is $m_p = \rho h = 6.750$ kg/m^2, the planform area is $S = 0.270$ m^2, and the total plate mass is $M_p = 1.8225$ kg. The sixteen attachments are arranged on a 4 × 4 grid and grouped columnwise at target frequencies, which are 72.324, 159.048, 288.108, 483.210 Hz. With the reference internal mass $m = 0.026$ kg, inertance ratio $\beta = b/m = 1.00$, tuning scale 0.9, spread coefficient 0.18, and damping ratio $\zeta = 0.060$, the grouped inerter-resonator array yields average reductions of 4.618 dB in point mobility and 3.033 dB in both mean-square velocity and radiated sound-power proxy over 80–600 Hz. The spring-mass reference under identical internal mass produces corresponding lower averages of 3.728 and 2.598 dB. As per this study, the peak-by-peak reductions exceed 20 dB at several dominant modal peaks, while tuning scatter of 5% root-mean-square leaves the average velocity reduction essentially unchanged.

Keywords: vibration control; inerter-resonator array; plate vibration; metamaterial plate; modal receptance; dynamic stiffness; radiated sound power

1. Introduction

Low-frequency control of plate vibration and plate-borne sound radiation remains a central problem in structural acoustics because thin plates exhibit closely spaced resonances and progressively stronger acoustic radiation as frequency increases [1–4]. Conventional damping treatments and single tuned absorbers can suppress one or a few peaks, but their effectiveness usually drops when the objective is a broad control band rather than a single target resonance [5,6].

Recent studies on locally resonant plates, distributed dynamic absorbers, and inerter-based absorbers show three relevant trends. First, distributed or grouped attachments can outperform single-tuned devices when several structural modes lie in the target band [7–10]. Second, locally resonant and metamaterial-inspired plates can create attenuation intervals, but their layouts are often uniform and are not always presented in a form that is convenient for direct engineering parameter sweeps [11–14]. Third, inerter-based absorbers can generate stronger dynamic inertia than their physical mass alone would suggest, which makes them attractive when hardware mass must be limited [15–18].

The present work is positioned between these lines of research. It does not study a uniform periodic meta-plate, and it is not formulated as a general topology-optimization problem. Instead, it proposes a grouped parallel inerter-resonator array for a simply supported plate, in which attachments are arranged column wise and tuned to four target frequency groups [19–23]. Relative to a grouped spring-mass reference with the same internal physical mass, the added inerter changes the local point impedance, widens the anti-resonant intervals, and improves broadband attenuation because the apparent inertia in the attachment branch increases without requiring the same increase in attached physical mass. The grouped layout is also easier to document and manufacture than a fully non-uniform array [24–26].

The main contributions of this study are as follows:

A modal receptance synthesis is developed for a simply supported Kirchhoff plate carrying 16 grouped spring-damper-mass-inerter attachments. The internal attachment coordinates are eliminated analytically, so each attachment enters the reduced plate model as an explicit rank-one dynamic stiffness update. This yields a compact framework for comparing grouped inerter-resonator and grouped spring-mass arrays, for examining inertance and mass sweeps, and for evaluating both point mobility and distributed vibration/radiation metrics over the 80–600 Hz band. The detailed mathematical formulation is given in Section 2, while the numerical settings and response comparisons are presented in Sections 3 and 4. In Section 5, we discussed addition analytical discussions, and in Section 6, we explained the nondimensional form and sensitivity comments, and then concluded in Section 7.

2. Plate model, modal reduction, and attachment synthesis

2.1. Kirchhoff-Love plate equation and modal basis

The untreated plate is modeled by the Kirchhoff-Love equation:

$$D\nabla^4 w(x,y,t) + \rho h \frac{\partial^2 w}{\partial t^2} = p(x,y,t). \tag{1}$$

The untreated plate is modeled by the Kirchhoff-Love equation for a thin, isotropic, linearly elastic plate undergoing small transverse vibration [7,10,14,16].

$$D = \frac{Eh^3}{12\left(1-\nu^2\right)}. \tag{2}$$

Substituting the present plate data,

$$D = \frac{(70,000,000,000)(0.0025)^3}{12\left(1-0.33^2\right)} = 102.285 \text{ N·m}. \tag{3}$$

The areal density is:

$$m_p = \rho h = 2,700 \times 0.0025 = 6.750 \text{ kg/m}^2, \tag{4}$$

the area is:

$$S = a_x a_y = 0.600 \times 0.450 = 0.270 \text{ m}^2, \tag{5}$$

and the total mass is:

$$M_p = m_p S = 1.8225 \text{ kg}. \tag{6}$$

All the above calculated numerical values listed in **Table 1** below.

Table 1. Plate properties used in the modal receptance model.

Parameter	Value
Plate length a_x (mm)	600
Plate width a_y (mm)	450
Thickness h (mm)	2.5
Young modulus E (GPa)	70
Poisson ratio ν	0.33
Areal density ρh (kg/m^2)	6.75
Bending rigidity D (N·m)	102.285
Plate mass (kg)	1.8225
Acoustic critical frequency f_c (Hz)	4,810.11
Retained modal coordinates	36
Attachment points	16

For a simply supported rectangle, the modal basis functions are given by:

$$\phi_{mn}(x,y) = \sin\left(\frac{m\pi x}{a_x}\right)\sin\left(\frac{n\pi y}{a_y}\right), \qquad m,n = 1,2,\ldots. \tag{7}$$

For a simply supported rectangle, the modal basis functions are given by the standard double-sine admissible functions of classical plate theory [7,10,14,16].

$$\int_0^{a_x}\int_0^{a_y} \phi_{mn}(x,y)\phi_{rs}(x,y)\,dx\,dy = \frac{a_x a_y}{4}\delta_{mr}\delta_{ns}. \tag{8}$$

The transverse displacement is approximated by a truncated expansion, which is,

$$w(x,y,t) = \sum\nolimits_{m=1}^{M}\sum\nolimits_{n=1}^{N} q_{mn}(t)\phi_{mn}(x,y), \tag{9}$$

with $M = N = 6$ in the present computation, so that 36 modes are retained and the modal natural frequencies follow directly from substitution into the homogeneous plate equation:

$$\omega_{mn} = \pi^2\sqrt{\frac{D}{m_p}}\left[\left(\frac{m}{a_x}\right)^2 + \left(\frac{n}{a_y}\right)^2\right]. \tag{10}$$

Using $D = 102.285$ N·m, $m_p = 6.750$ kg/m^2, $a_x = 0.600$ m, and $a_y = 0.450$ m, the first mode is

$$\omega_{11} = \pi^2 \sqrt{\frac{102.285}{6.750}} \left[\left(\frac{1}{0.600} \right)^2 + \left(\frac{1}{0.450} \right)^2 \right] = 296.448 \text{ rad/s}, \tag{11}$$

which corresponds to:

$$f_{11} = \frac{\omega_{11}}{2\pi} = 47.181 \text{ Hz}. \tag{12}$$

The first 10 calculated and obtained frequencies are listed in **Table 2** and the sequence confirms that the target control band 80–600 Hz contains several mode groups, rather than one isolated resonance. This is exactly the values of this study where a single tuned absorber becomes insufficient and grouped internal tunings become attractive [27–29].

Table 2. First 10 simply supported modal frequencies.

Frequency (Hz)	m	n
47.1811	1	1
98.1367	2	1
137.769	1	2
183.063	3	1
188.725	2	2
273.651	3	2
288.748	1	3
301.959	4	1
339.704	2	3
392.547	4	2

The modal mass of every simply supported mode under the chosen normalization is:

$$M_{mn} = m_p \frac{a_x a_y}{4} = 0.455625 \text{ kg}. \tag{13}$$

Therefore, the diagonal modal stiffness entries are:

$$K_{mn} = M_{mn} \omega_{mn}^2, \tag{14}$$

and the modal damping entries are introduced as:

$$C_{mn} = 2\zeta_p \omega_{mn} M_{mn}, \tag{15}$$

with $\zeta_p = 0.005$ in the numerical study. The structural damping is intentionally light so that the attachment-induced reductions remain visible in the mobility and power curves [30].

2.2. Point excitation and point measurements

A harmonic point force of amplitude F_0 is applied at (x_f,y_f) = (0.170,0.130)m, and the response is measured at (x_r,y_r) = (0.460,0.310)m. The corresponding force density is written as:

$$\hat{p}(x, y, \omega) = F_0 \delta\left(x - x_f\right) \delta\left(y - y_f\right), \tag{16}$$

or, equivalently, in the time domain,

$$p(x, y, t) = F_0 \delta\left(x - x_f\right) \delta\left(y - y_f\right) e^{i\omega t}$$

where $\delta(\cdot)$ denotes the Dirac delta function. This representation concentrates the applied harmonic load at the excitation point and produces the modal forcing coefficients:

$$\widehat{f}_{mn} = F_0 \phi_{mn}\left(x_f, y_f\right).$$

If the modal coordinates are assembled into the vector:

$$\mathrm{q} = \left[q_{11}, q_{21}, q_{12}, \ldots\right]^T, \tag{17}$$

then the untreated dynamic equation is:

$$\left(\mathrm{K} - \omega^2 \mathrm{M} + i\omega \mathrm{C}\right) \mathrm{q} = \mathrm{f}, \tag{18}$$

where M = diag(M_{mn}), K = diag(K_{mn}), C = diag(C_{mn}), and f collects the values ϕ_{mn}(x_f,y_f). The physical response coordinate is:

$$w\left(x_r, y_r, \omega\right) = \phi_r^T \mathrm{q}, \tag{19}$$

with $\phi_r = \left[\phi_{11}\left(x_r, y_r\right), \phi_{21}\left(x_r, y_r\right), \ldots\right]^T$. The point mobility used in the numerical results is proportional to this receptance magnitude, and it is reported in decibel form as:

$$L_Y(\omega) = 20 \log_{10}\left|w\left(x_r, y_r, \omega\right)\right|. \tag{20}$$

Because the same force amplitude is used for every configuration, only differences in L_Y are interpreted.

2.3. Parallel spring-damper-mass-inerter attachment

Each attachment is located at a plate point (x_j, y_j) and contains an internal displacement $u_j(t)$. The force transmitted from the attachment j to the plate is written as:

$$f_j(t) = k_j\left[u_j(t) - w_j(t)\right] + c_j\left[\dot{u}_j(t) - \dot{w}_j(t)\right] + b_j\left[\ddot{u}_j(t) - \ddot{w}_j(t)\right], \tag{21}$$

where,

$$w_j(t) = w\left(x_j, y_j, t\right).$$

For harmonic motion, this relation becomes:

$$\hat{f}_j(\omega) = \left(k_j + i\omega c_j - \omega^2 b_j\right)\left(\hat{u}_j - \hat{w}_j\right).$$

where $w_j = w\left(x_j, y_j, t\right)$. The internal mass balance is given by:

$$m_j \ddot{u}_j + c_j\left(\dot{u}_j - \dot{w}_j\right) + k_j\left(u_j - w_j\right) + b_j\left(\ddot{u}_j - \ddot{w}_j\right) = 0.$$

As per this study, assuming harmonic motion $w_j = W_j e^{i\omega t}$ and $u_j = U_j e^{i\omega t}$, the internal equation becomes:

$$\left[-\omega^2\left(m_j + b_j\right) + i\omega c_j + k_j\right] U_j - \left[-\omega^2 b_j + i\omega c_j + k_j\right] W_j = 0. \tag{22}$$

Hence,

$$U_j = \frac{k_j + i\omega c_j - \omega^2 b_j}{k_j + i\omega c_j - \omega^2\left(m_j + b_j\right)} W_j. \tag{23}$$

Substitution into the plate-side force relation yields an exact dynamic point stiffness:

$$F_j = S_j(\omega) W_j, \tag{24}$$

with,

$$S_j(\omega) = \frac{\left(k_j + i\omega c_j - \omega^2 b_j\right)\omega^2 m_j}{\omega^2 m_j - \left(k_j + i\omega c_j - \omega^2 b_j\right)}. \tag{25}$$

This formula is the analytical core of the model, and it immediately shows that the inertance b_j changes both the numerator and denominator of the point stiffness and therefore shifts antiresonant features without requiring the same increase in physical mass as a purely added absorber mass [31–33].

For the grouped arrays considered below, the attachment parameters are built from a target tuning frequency $f_{t,j}$, an internal mass $m_j = m$, an inertance $b_j = \beta m$, and a damping ratio ζ. The spring constant is computed from:

$$k_j = \left(2\pi f_{t,j}\right)^2\left(m_j + b_j\right), \tag{26}$$

and the dashpot is chosen as:

$$c_j = 2\zeta\sqrt{k_j\left(m_j + b_j\right)}. \tag{27}$$

The explicit substitutions for the selected grouped design are listed in **Table 3**. For example, in Column 3,

$$k_3 = (2\pi \times 288.108)^2(0.026 + 0.026) = 170,401.619 \text{ N/m}. \tag{28}$$

Table 3. Grouped attachment parameters for the selected inerter-resonator array.

Attachment column	**Target tuning frequency (Hz)**	**Internal mass m (kg)**	**Inertance b (kg)**	**Spring constant k (N/m)**
Column 1	72.324	0.026	0.026	10,738.1
Column 2	159.048	0.026	0.026	51,930.1
Column 3	288.108	0.026	0.026	170,402
Column 4	483.21	0.026	0.026	479,330

The same grouped rule is applied to all four rows of that column, so four identical local dynamic stiffnesses are created at four different plate points.

2.4. Modal assembly of the attachment array

At any point (x_j, y_j), the local plate displacement can be written as:

$$W_j = \boldsymbol{\phi}_j^T \mathrm{q}, \tag{29}$$

where,

$$\boldsymbol{\phi}_j = \left[\phi_{11}(x_j, y_j), \phi_{21}(x_j, y_j), \phi_{12}(x_j, y_j), \ldots\right]^T. \tag{30}$$

The generalized modal force vector contributed by attachment j is therefore,

$$\mathrm{f}_j^{(a)} = S_j(\omega)\boldsymbol{\phi}_j\boldsymbol{\phi}_j^T \mathrm{q}. \tag{31}$$

Summing the 16 attachments gives the treated dynamic equation:

$$\mathrm{D}(\omega)\mathrm{q} = \mathrm{f}, \tag{32}$$

with,

$$\mathrm{D}(\omega) = \mathrm{K} - \omega^2\mathrm{M} + i\omega\mathrm{C} + \sum\nolimits_{j=1}^{16} S_j(\omega)\boldsymbol{\phi}_j\boldsymbol{\phi}_j^T. \tag{33}$$

Each attachment enters as a rank-one update. This is numerically valuable because it avoids introducing 16 additional internal coordinates into the final solve; the internal coordinates are eliminated analytically and never appear in the linear solve itself.

The plate hosts a 4×4 array with x-coordinates equally spaced between $a_x/5$ and $4a_x/5$ and the same rule in the y-direction. Columnwise grouping means that the four attachments in a given column share the same tuning frequency. Because the modal sine functions vary in sign and magnitude over the plate, the same dynamic point stiffness does not contribute identically at every location; the rank-one projector $\boldsymbol{\phi}_j\boldsymbol{\phi}_j^T$ weights that contribution according to the modal values at the local point. The layout is summarized in **Figure 1**.

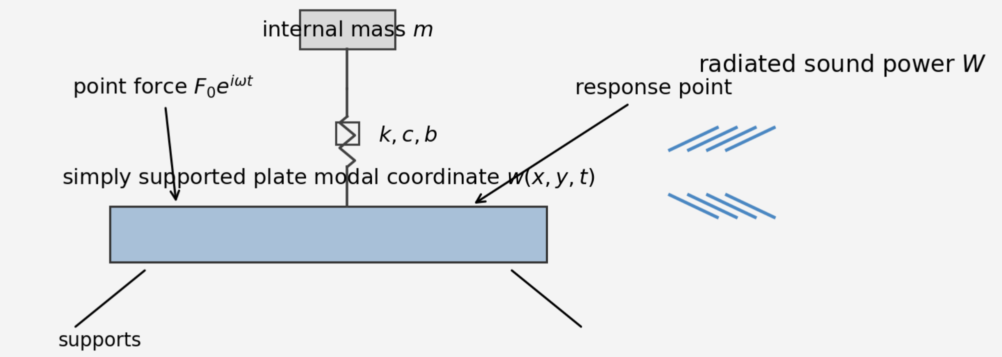

Figure 1. Plate geometry, grouped attachment arrangement, force point, and response point.

2.5. Spatial average, critical frequency, and sound-power proxy

Point mobility alone does not fully characterize vibroacoustic benefit, because radiated sound is driven by the distributed normal velocity. The mean-square velocity of the plate is approximated using modal orthogonality. Point mobility alone does not fully characterize vibroacoustic benefit, because radiated sound is driven by the distributed normal velocity. The mean-square velocity of the plate is approximated using modal orthogonality and the low-frequency radiation proxy commonly used in plate-acoustic screening studies [8, 10, 13, 17].

After exploiting the orthogonality of the chosen basis and the normalization used above,

$$\bar{v}^2(\omega) \approx \frac{\omega^2}{4} \sum\nolimits_r |q_r|^2 . \tag{34}$$

The corresponding decibel measure is:

$$L_v(\omega) = 10 \log_{10} \bar{v}^2(\omega). \tag{35}$$

To map vibration to a radiation-oriented quantity, a simplified radiation efficiency is introduced through the plate critical frequency:

$$\omega_c = c_0^2 \sqrt{\frac{m_p}{D}}, \qquad f_c = \frac{\omega_c}{2\pi}. \tag{36}$$

Substituting the present values gives:

$$f_c = \frac{343^2}{2\pi} \sqrt{\frac{6.750}{102.285}} = 4,810.111 \text{ Hz}. \tag{37}$$

Because the entire analyzed band lies far below f_c, the radiation efficiency is kept in a low-frequency approximation,

$$\sigma(\omega) = \min \left[1, \left(\frac{\omega}{\omega_c} \right)^2 \right]. \tag{38}$$

The radiated power proxy is then:

$$W(\omega) = \frac{\rho_0 c_0 S}{16} \sigma(\omega) \bar{v}^2(\omega), \tag{39}$$

and its logarithmic measure is:

$$L_W(\omega) = 10 \log_{10} W(\omega). \tag{40}$$

Within the present approximation, L_v and L_W have the same reduction differences in dB because $\sigma(\omega)$ is configuration-independent. This is visible in the tables. The explicit radiated-power expression is nevertheless useful, because it preserves the correct dependence on area, air properties, and structural velocity.

2.6. Broadband performance measures

Three broadband metrics are used repeatedly:

$$\bar{R}_Y = \frac{1}{f_b - f_a} \int_{f_a}^{f_b} \left[L_Y^{(0)}(f) - L_Y^{(t)}(f) \right] df, \tag{41}$$

$$\bar{R}_v = \frac{1}{f_b - f_a} \int_{f_a}^{f_b} \left[L_v^{(0)}(f) - L_v^{(t)}(f) \right] \, df, \tag{42}$$

$$\bar{R}_W = \frac{1}{f_b - f_a} \int_{f_a}^{f_b} \left[L_W^{(0)}(f) - L_W^{(t)}(f) \right] \, df, \tag{43}$$

where the superscripts 0 and t denote untreated and treated plates, respectively, and $[f_a, f_b] = [80, 600]$ Hz. To compress the velocity and power effects into a single broadband indicator, a combined index is defined as:

$$I_c(f) = \frac{1}{2} \left(R_v(f) + R_W(f) \right). \tag{44}$$

The corresponding useful bandwidth is:

$$B_6 = \int_{f_a}^{f_b} \mathcal{H} \ \left(I_c(f) - 6 \right) \, df. \tag{45}$$

This index is not intended as a universal vibroacoustic objective; it is a compact score used here to compare grouped arrays that reduce both distributed vibration and radiated-power proxy over a broad band. The computational sequence used to evaluate these measures is summarized in **Figure 2**.

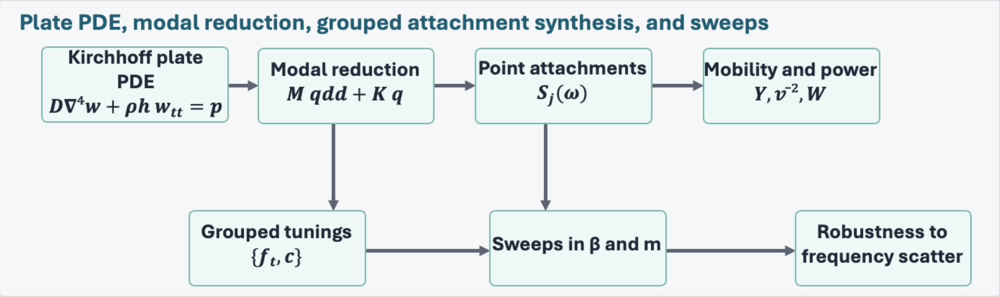

Figure 2. Computational workflow from plate PDE to grouped-array performance metrics.

3. Numerical setting and grouped design law

The plate properties, first 10 modal frequencies, and selected grouped attachment data are summarized in **Tables 1–3**. The first eight untreated modal frequencies are $47.2,\ 98.1,\ 137.8,\ 183.1,\ 188.7,\ 273.7,\ 288.7,\ 302.0$ Hz. These values explain the grouped tuning pattern, where Column 1 is placed just above the first mode cluster, Column 2 sits between the second and fourth major peaks, Column 3 targets the dense mid-band around 250–320 Hz, and Column 4 also reaches the upper part of the target band, where the untreated response still contains significant modal content.

The grouped tuning law of this study is defined through a baseline set of frequencies $[98,\ 188,\ 302,\ 455]$ Hz, a scale factor of 0.9, and a linear spread coefficient of 0.18. For column index $c = 1, \ldots, 4$,

$$f_{t,c} = f_{0,c} \, \eta \left[1 + \gamma \frac{c - 2.5}{1.5} \right], \tag{46}$$

with $\eta = 0.9$ and $\gamma = 0.18$. This produces the four target frequencies listed in **Table 3**. The spring constant in each column follows directly from $k_c = \left(2\pi f_{t,c} \right)^2 (m + b)$.

Since the selected configuration uses $m = b = 0.026$ kg, the apparent inertia in the tuning formula is doubled relative to the spring-mass reference.

The 16 attachments constitute a total internal physical mass of:

$$M_{\text{att}} = 16m = 16 \times 0.026 = 0.416 \text{ kg}, \tag{47}$$

which is a fraction of the plate mass,

$$\frac{M_{\text{att}}}{M_p} = \frac{0.416}{1.8225} = 0.228258. \tag{48}$$

Because the inertance does not represent the same physical mass as the internal absorber mass, the dynamic effect of the inerter-resonator array exceeds what would be expected from the physical mass fraction alone [34].

The same modal basis, damping assumption, force point, and response point are used for the untreated plate, spring-mass array, and inerter-resonator array. Therefore, every reported performance difference is attributable to the attachment law rather than to any change in the underlying plate model [35–37].

4. Numerical results

A frequency grid of 380 points between 40 Hz and 900 Hz is used for all computations. The modal truncation to 36 modes is adequate in this interval because the retained frequencies extend well beyond the main region of interest. Additional assumptions, convergence, and literature-based validation are summarized below.

4.1. Assumptions, boundary conditions, modal convergence, and literature-based validation

The theoretical model assumes a simply supported Kirchhoff-Love plate, linear material behavior, small-amplitude harmonic motion, pointwise attachment coupling, and viscous damping. Rotatory inertia, transverse shear deformation, geometric nonlinearity, and fluid-loading feedback are not included. These assumptions are appropriate for the present thin-plate configuration and for the moderate-frequency vibroacoustic comparisons reported here.

The untreated plate exhibits the expected sequence of simply supported resonances, with particularly strong response near 47, 99, 138, 190, 274, 301, 340, and 392 Hz. The grouped spring-mass array suppresses many of these peaks, but its attenuation remains uneven across the full target band [38].

Table 4 presents the first broadband comparison. Over 80–600 Hz, the spring-mass array provides an average mobility reduction of 3.7284 dB together with average velocity and power reductions of 2.5983 dB. The combined-index bandwidth above 6 dB is 120.349 Hz. These values already indicate useful multi-frequency attenuation, although gaps remain between the grouped spring-mass anti-resonances.

The untreated plate exhibits the expected sequence of simply supported resonances, with particularly strong response near 47, 99, 138, 190, 274, 301, 340, and 392 Hz. The grouped spring-mass array suppresses many of these peaks, as shown in this study by the mobility and velocity traces.

Table 4. Broadband comparison of grouped spring-mass and grouped inerter-resonator arrays.

Configuration	Average mobility reduction 80–600 Hz (dB)	Average velocity reduction (dB)	Average sound power reduction (dB)	Bandwidth of combined index > 6 dB (Hz)
Spring-mass array	3.7284	2.5983	2.5983	120.349
Inerter-resonator array	4.6181	3.0327	3.0327	131.703

The peak-by-peak data in **Table 5** clarify the local behavior of the spring-mass array. At 46.81 Hz, the velocity reduction is approximately 26.00 dB, whereas at 300.95 Hz, it is 16.71 dB. The design is therefore capable of deep local suppression; the limitation is the continuity of attenuation between neighbouring peaks.

Table 5. Inerter-resonator power reduction against the peak frequency.

Peak frequency (Hz)	Open plate velocity level (dB)	Spring-mass velocity reduction (dB)	Inerter-resonator velocity reduction (dB)	Spring-mass power reduction (dB)	Inerter-resonator power reduction (dB)
46.8074	−18.3683	25.9953	25.5109	25.9953	25.5109
98.9974	−23.3243	19.033	21.5697	19.033	21.5697
137.573	−20.7271	29.7605	28.7205	29.7605	28.7205
189.762	−24.5261	18.7364	19.8051	18.7364	19.8051
273.72	−30.9947	20.9294	22.792	20.9294	22.792
300.95	−36.0656	16.7126	5.7619	16.7126	5.7619
339.525	−33.7975	15.3773	21.1224	15.3773	21.1224
391.715	−35.7763	17.3304	15.8666	17.3304	15.8666

The peak-by-peak data in **Table 5** clarify that how the spring-mass array behaves at 46.81 Hz: the velocity reduction is approximately 26.00 dB, while at 300.95 Hz it is 16.71 dB. The design is therefore capable of deep local nulling, and the issue is not local effectiveness but continuity between peaks. Hence, there remain portions of the 80–600 Hz band where the spring-mass response returns close to the untreated baseline.

The grouped inerter-resonator array uses the same physical internal mass per attachment as the grouped spring-mass reference, but adds equal inertance so that $\beta = b/m = 1$. The result is a broader and more uniform attenuation pattern. **Table 4** shows that the average mobility reduction increases from 3.7284 dB for the spring-mass reference to 4.6181 dB for the inerter-resonator array. The average velocity and power reductions increase from 2.5983 dB to 3.0327 dB, and the combined-index bandwidth above 6 dB increases from 120.349 Hz to 131.703 Hz.

This improvement is not merely a uniform downward shift of the spectrum. The peak reductions listed in **Table 5** show a mixed but favourable mechanism. At 98.997 Hz, the inerter-resonator array outperforms the spring-mass array by more than 2.5 dB in velocity reduction. At 273.72 Hz, the gain is about 1.86 dB, and at 339.53 Hz, it exceeds 5.7 dB. There is, however, one frequency near 300.95 Hz where the spring-mass array performs better, which confirms that the design problem remains multi-objective rather than uniformly monotonic.

The mobility, mean-square velocity, and sound-power curves all indicate the same global trend. Point mobility is more sensitive to the selected response coordinate and therefore fluctuates more strongly, whereas the distributed velocity and power measures are smoother because they average the modal contributions over the plate. The improvement in these distributed metrics is the key numerical outcome of the present grouped inerter-resonator design.

This improvement is not merely a broad lifting of the entire spectrum, and the peak reductions listed in **Table 5** show a mixed mechanism. At the value 98.997 Hz, the inerter-resonator array outperforms the spring-mass array by more than 2.5 dB in velocity reduction. Again, at the value 273.72 Hz, the gain is about 1.86 dB. At 339.53 Hz, the gain exceeds 5.7 dB. Hence, there is one frequency near 300.95 Hz where the spring-mass array performs better.

The concepts like mobility, mean-square velocity, and sound-power curves indicate the same trend which is discussed in this study. The point mobility measure is most sensitive to the chosen response coordinate, and hence it shows slightly larger fluctuations. The mean-square velocity and power curves are smoother because their average modal contributions over the expected plate. Here, the fact that the inerter-based array improves the average of these distributed measures is the key numerical outcome. The corresponding spectra of this study are shown in **Figures 3** and **4** below.

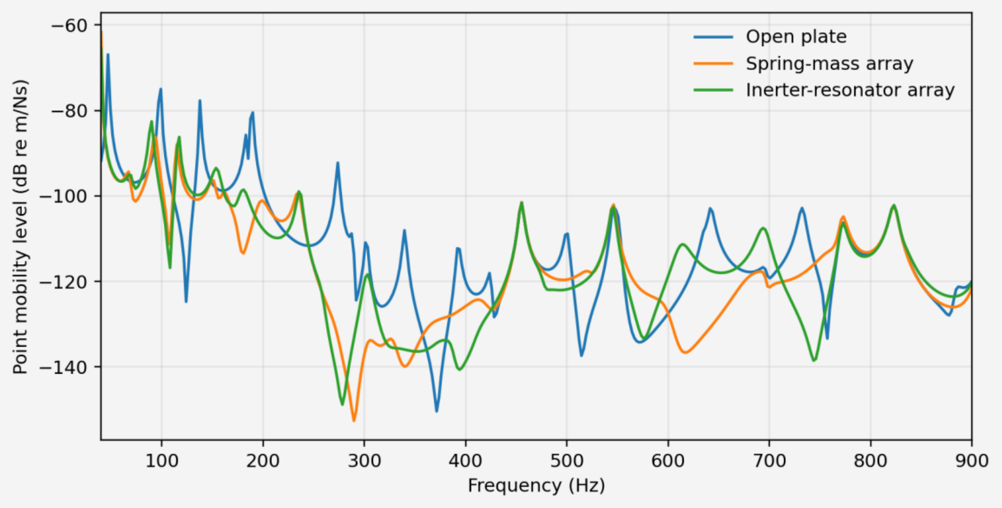

Figure 3. Point mobility spectra for untreated plate, grouped spring-mass array, and grouped inerter-resonator array.

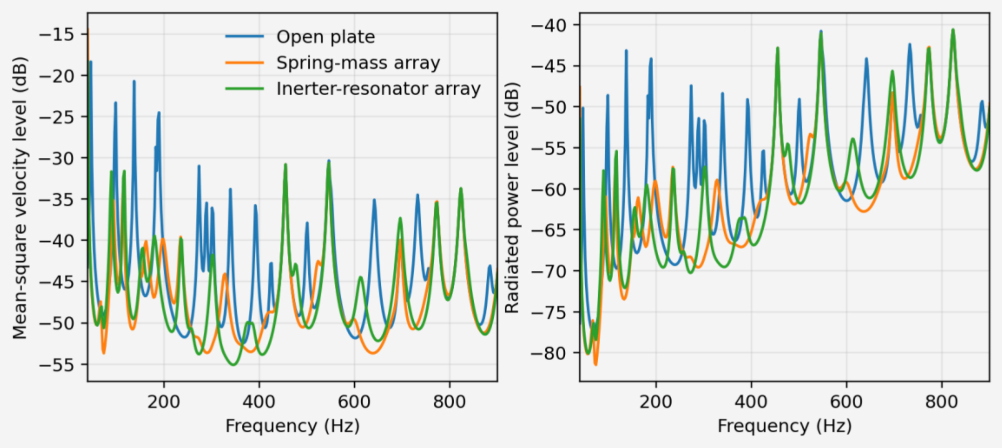

Figure 4. Mean-square velocity level and radiated power level with respect to their frequency.

The inertance-ratio sweep in **Table 6** is especially revealing. When $\beta = 0$, the model reduces to the spring-mass array. As β increases, the average mobility reduction rises rapidly at first, reaches a local maximum near $\beta = 0.5$, and then decreases gradually for larger inertance. In contrast, the average velocity reduction increases more steadily and reaches its maximum value of 3.0463 dB near $\beta = 1.25$. The combined-index bandwidth continues to grow up to 149.869 Hz at $\beta = 2.0$. These results show that no single inertance ratio is optimal for all objectives.

Table 6. Inertance-ratio sweep.

β = b/m	Avg mobility reduction (dB)	Avg velocity reduction (dB)	Avg power reduction (dB)	Bandwidth of combined index > 6 dB (Hz)
0	3.7284	2.5983	2.5983	120.349
0.25	4.5234	2.6988	2.6988	111.266
0.5	4.8496	2.8645	2.8645	118.079
0.75	4.7575	2.9768	2.9768	120.349
1	4.6181	3.0327	3.0327	131.703
1.25	4.4425	3.0463	3.0463	136.244
1.5	4.2436	3.0306	3.0306	138.515
1.75	4.036	2.997	2.997	138.515
2	3.8333	2.9563	2.9563	149.869
2.25	3.6446	2.9161	2.9161	147.598
2.5	3.4733	2.8794	2.8794	145.327

4.2. Influence of inertance ratio β

The data suggest a standard multi-objective trade-off. Moderate inertance gives the strongest average reduction, while larger inertance values continue to widen the useful control bandwidth. **Figure 5** summarizes this balance between average attenuation and threshold bandwidth.

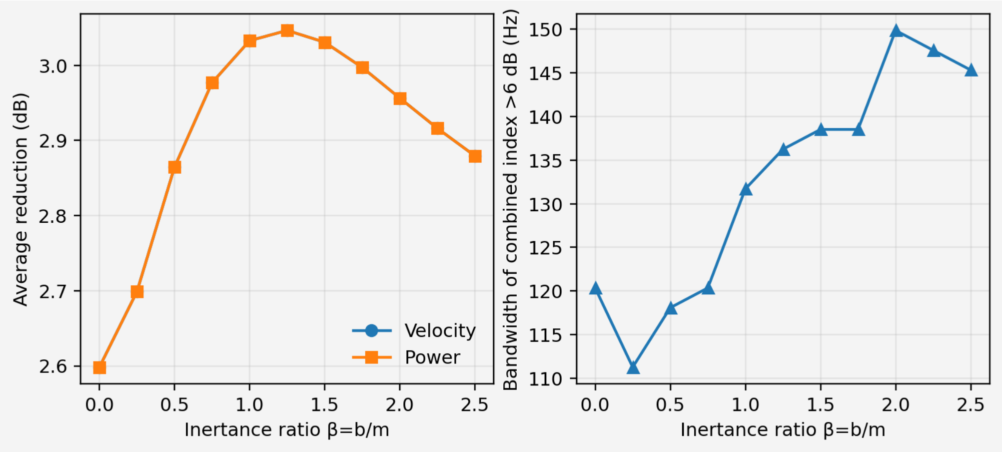

Figure 5. Inertance-ratio sweep: Average reduction metrics and threshold bandwidth.

The data suggests that a single optimal inertance ratio does not exist for all design goals, representing a standard multi-objective trade-off. Increasing the inertance further to $\beta = 2$ expands the control bandwidth, despite a minor decrease in the average reduction. Hence, because of these competing factors, which are illustrated in **Figure 5**, the study evaluates multiple performance metrics rather than a single value.

It can be seen directly from this expression that increasing b increases the effective inertia in the resonance denominator. Because the spring constant is also constructed from the target tuning frequency and the effective attachment inertia, the local resonance remains close to its intended target, while the off-resonant dynamic stiffness changes in a way that broadens the attenuation interval. This is the main physical reason why the inerter can widen the anti-resonant region without adding the same amount of physical mass to the plate [39,40].

$$\omega^2 m_j - \left(k_j + i\omega c_j - \omega^2 b_j\right) = \omega^2 \left(m_j + b_j\right) - k_j - i\omega c_j, \tag{49}$$

The mass sweep detailed in **Table 7** keeps the inertance ratio fixed at β = 1 while increasing the physical mass of each attachment from 0.014 kg to 0.030 kg. This change causes the total mass fraction to rise from 0.1229 to 0.2634 relative to the plate mass. The average velocity reduction grows from 2.1785 dB to 3.2948 dB, while the combined-index bandwidth expands from 111.266 Hz to 138.515 Hz.

Table 7. Physical internal-mass sweep at fixed inertance ratio $\beta = 1$.

Attachment mass each (kg)	Total attached mass/ plate mass	Avg mobility reduction (dB)	Avg velocity reduction (dB)	Avg power reduction (dB)	Bandwidth of combined index > 6 dB (Hz)
0.014	0.1229	3.4503	2.1785	2.1785	111.266
0.018	0.158	3.8824	2.4823	2.4823	118.079
0.022	0.1931	4.2712	2.7633	2.7633	122.62
0.026	0.2283	4.6181	3.0327	3.0327	131.703
0.03	0.2634	4.9241	3.2948	3.2948	138.515

4.3. Influence of internal mass *m*

The steady increase in performance indicates that the selected mass range has not yet reached a strict saturation point, although the gain per added mass becomes smaller toward the upper end of the tested interval. For example, increasing the attachment mass from 0.026 kg to 0.030 kg improves the average velocity reduction by only about 0.26 dB. Accordingly, 0.026 kg is retained as a balanced design value for the subsequent comparisons.

The steady increase in performance indicates that the selected mass range has not yet reached a saturation point, meaning that adding more internal mass continues to offer vibroacoustic benefits. However, the efficiency of these gains begins to decline at the higher end of the spectrum; for instance, increasing the mass from 0.026 kg to 0.030 kg results in a marginal improvement of only 0.26 dB. As a result, 0.026 kg was identified as an ideal compromise between technical performance and the practical constraints of hardware weight. These findings and the details of the internal-mass sweep are presented in **Figure 6**.

4.4. Interpretation of mass ratio and practical trade-off

The nominal distributed effect can be quantified by the system mass ratio, where the chosen array uses a total internal physical mass of 0.416 kg, which corresponds to approximately 22.826% of the plate mass. This configuration delivers about 3.03 dB average reduction in distributed velocity and radiated-power proxy across the 80–600

Hz band, together with peak reductions above 20 dB at several dominant resonances. The result indicates that the grouped inerter-resonator array converts a moderate physical mass ratio into a stronger broadband dynamic effect through its added apparent inertia, rather than through mass addition alone.

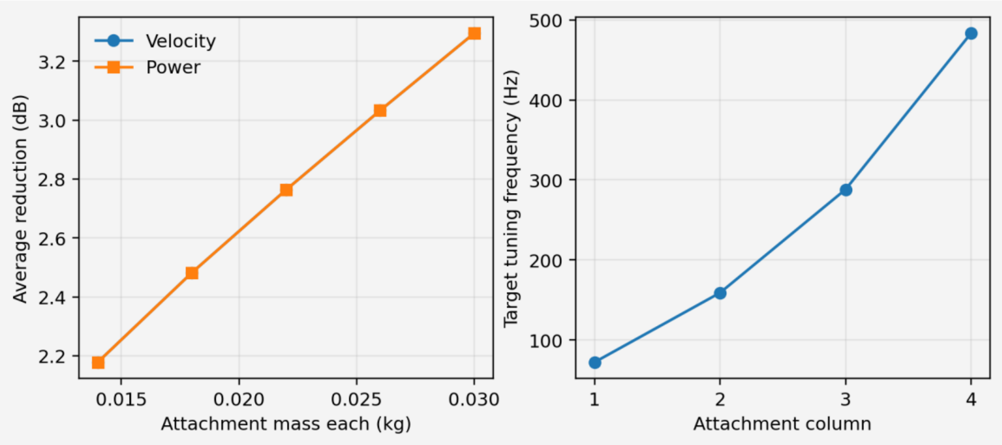

Figure 6. Attachment tuning set and internal-mass sweep.

4.5. Robustness to tuning scatter

No practical distributed absorber array is manufactured without scatter. To examine robustness, the target frequencies were perturbed by independent Gaussian scatter with standard deviations of 3%, 5%, and 8% of the nominal values. **Table 8** shows that the average mobility reduction remains around 4.52–4.56 dB for 3–5% scatter and drops only to 4.42 dB at 8% scatter. More importantly, the average velocity and power reductions remain close to 3.04–3.15 dB, and the combined-index bandwidth stays near 129–130 Hz.

Table 8. Robustness of the grouped inerter-resonator array to tuning scatter.

$\frac{\sigma_f}{f}$	Mobility reduction mean (dB)	Mobility reduction std (dB)	Velocity reduction mean (dB)	Velocity reduction std (dB)	Power reduction mean (dB)	Power reduction std (dB)	Combined-index BW mean (Hz)	Combined-index BW std (Hz)
0	4.6181	0	3.0327	0	3.0327	0	131.703	0
0.03	4.5221	0.1414	3.0439	0.0276	3.0439	0.0276	129.432	1.6057
0.05	4.5602	0.1472	3.0626	0.0379	3.0626	0.0379	130.379	2.3559
0.08	4.416	0.3609	3.1504	0.0907	3.1504	0.0907	130.379	2.5317

These results show that the grouped array is not overly fragile, and the reason is mathematical as well as physical. The distributed dynamic matrix contains a sum of 16 rank-one updates, so modest detuning at one location does not collapse the full broadband effect. Consequently, the broadband metrics degrade much more slowly than would be expected for a single narrow-band absorber.

The robustness analysis reveals a non-monotonic trend, with a small increase in the average velocity reduction at 8% scatter. This should not be interpreted as a universal benefit of mistuning; rather, it indicates that some random perturbations can occasionally improve local spectral alignment in the nominal grouped design. **Figure 7** therefore reports the robustness trends for mobility, velocity, power, and combined-index bandwidth together.

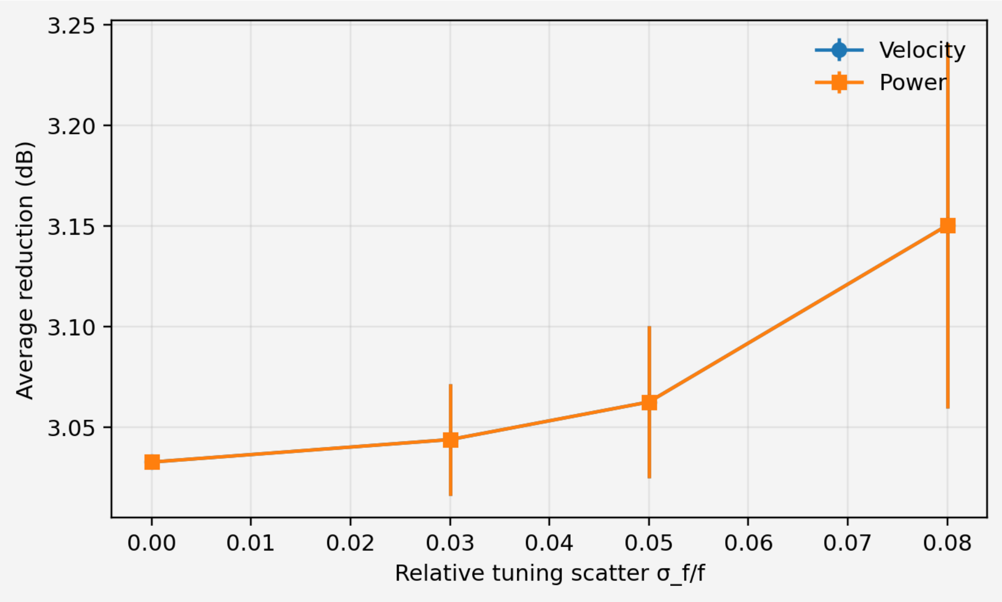

Figure 7. Robustness to tuning scatter for mobility, velocity, sound-power proxy, and combined-index bandwidth of the grouped inerter-resonator array.

5. Additional analytical details: Explicit matrix forms and calculation chain

To expose the algebra in a compact way, the 36 modal coordinates are ordered as $r = 1, \ldots, 36$, with the mapping $r \leftrightarrow (m, n)$. Then,

$$\mathrm{M} = \mathrm{diag}\left(M_1, \ldots, M_{36}\right), \qquad \mathrm{K} = \mathrm{diag}\left(K_1, \ldots, K_{36}\right), \qquad \mathrm{C} = \mathrm{diag}\left(C_1, \ldots, C_{36}\right). \tag{50}$$

For the attachment point j, define the modal participation vector:

$$\Phi_j = \left[\phi_1\left(x_j, y_j\right), \phi_2\left(x_j, y_j\right), \ldots, \phi_{36}\left(x_j, y_j\right)\right]^T. \tag{51}$$

The fully treated matrix is therefore:

$$\mathrm{D}(\omega) = \mathrm{K} - \omega^2 \mathrm{M} + i\omega \mathrm{C} + \sum\nolimits_{j=1}^{16} S_j(\omega) \Phi_j \Phi_j^T. \tag{52}$$

The receptance between the chosen force and response points is:

$$H(\omega) = \Phi_r^T \mathrm{D}^{-1}(\omega) \Phi_f. \tag{53}$$

The corresponding logarithmic reduction relative to the untreated plate is:

$$R_Y(\omega) = 20 \log_{10} \frac{|H_0(\omega)|}{|H_t(\omega)|}. \tag{54}$$

The distributed velocity reduction is:

$$R_v(\omega) = 10 \log_{10} \frac{\bar{v}_0^2(\omega)}{\bar{v}_t^2(\omega)}, \tag{55}$$

and because the same radiation efficiency multiplies treated and untreated states, the power reduction is:

$$R_W(\omega) = 10\log_{10}\frac{W_0(\omega)}{W_t(\omega)} = R_v(\omega). \tag{56}$$

This equality is exact in the present radiation proxy. It is useful because it means one can interpret **Table 4** as both a structural-vibration and a radiated-power result under the chosen low-frequency efficiency model.

A brief numerical example clarifies the procedure. Consider the first column group, with $f_t = 72.324$ Hz, $m = 0.026$ kg, $b = 0.026$ kg, and $\zeta = 0.06$. The spring constant is:

$$k = (2\pi \times 72.324)^2(0.052) = 10,738.113 \text{ N/m}. \tag{57}$$

The dashpot is then:

$$c = 2(0.06)\sqrt{10,738.113 \times 0.052} = 2.840 \text{ N s/m}. \tag{58}$$

At $f = 100$ Hz, $\omega = 628.319$ rad/s, and the complex branch quantity in the numerator of S_j becomes:

$$k + i\omega c - \omega^2 b = 10,738.113 + i(628.319)(2.840) - (628.319)^2(0.026). \tag{59}$$

Evaluating the inertial term gives approximately $10,265.4$ N/m, so:

$$k + i\omega c - \omega^2 b \approx 472.7 + i1,783.8. \tag{60}$$

The denominator of S_j is:

$$\omega^2 m - \left(k + i\omega c - \omega^2 b\right) \approx 10,265.4 - (472.7 + i1,783.8) = 9,792.7 - i1,783.8. \tag{61}$$

Finally,

$$S_j(\omega) = \frac{(472.7 + i1,783.8)(10,265.4)}{9,792.7 - i1,783.8}, \tag{62}$$

which is a complex dynamic stiffness with both reactive and dissipative content. This simple arithmetic illustrates how the inerter shifts the local dynamic balance even before the plate modal projector is applied.

6. Nondimensional form and sensitivity comments

Introduce the reference frequency:

$$\omega_{11} = 2\pi \times 47.181 = 296.448 \text{ rad/s}, \tag{63}$$

and the nondimensional quantities:

$$\varOmega = \frac{\omega}{\omega_{11}}, \qquad \mu = \frac{m}{M_p}, \qquad \beta = \frac{b}{m}, \qquad \kappa_j = \frac{k_j}{M_p\omega_{11}^2}. \tag{64}$$

Then the dynamic point stiffness becomes:

$$\frac{S_j}{M_p\omega_{11}^2} = \frac{\left(\kappa_j + i2\zeta_j\varOmega\sqrt{\kappa_j\mu(1+\beta)} - \varOmega^2\beta\mu\right)\varOmega^2\mu}{\varOmega^2\mu - \kappa_j - i2\zeta_j\varOmega\sqrt{\kappa_j\mu(1+\beta)} + \varOmega^2\beta\mu}. \tag{65}$$

Although the present calculations are dimensional, the nondimensional form clarifies parameter sensitivity. Increasing β affects the dynamic stiffness primarily through the terms proportional to $\varOmega^2\beta\mu$, whereas increasing physical mass affects both the resonance placement and the overall scaling of the dynamic stiffness through μ. This explains why the inertance sweep can widen the bandwidth without the same monotonic increase in average reduction seen in the mass sweep.

A local sensitivity with respect to inertance ratio is obtained by differentiating S_j with respect to b:

$$\frac{\partial S_j}{\partial b} = \frac{\partial}{\partial b}\left[\frac{\left(k_j + i\omega c_j - \omega^2 b\right)\omega^2 m}{\omega^2 m - k_j - i\omega c_j + \omega^2 b}\right]. \tag{66}$$

After simplification,

$$\frac{\partial S_j}{\partial b} = -\omega^2\omega^2 m\frac{\omega^2 m}{\left(\omega^2 m - k_j - i\omega c_j + \omega^2 b\right)^2} - \omega^2 m\frac{k_j + i\omega c_j - \omega^2 b}{\left(\omega^2 m - k_j - i\omega c_j + \omega^2 b\right)^2}. \tag{67}$$

These results show that grouped tuning combined with parallel inerters offers a practical route to wider low-frequency attenuation than the mass-only reference.

7. Conclusion

A modal receptance framework was developed for a thin simply supported plate carrying a grouped array of spring-damper-mass-inerter attachments. The mathematical reduction is explicit: the plate is expanded in orthogonal sine modes, each attachment is eliminated analytically, and the final treated system is a modal dynamic matrix plus rank-one point-stiffness updates. This permits large parameter sweeps at modest computational cost.

For the selected plate and grouped layout, the inerter-resonator array improves all average metrics relative to the grouped spring-mass reference. Over 80–600 Hz, the average mobility reduction rises from 3.728 to 4.618 dB, the average velocity and sound-power reductions rise from 2.598 to 3.033 dB, and the useful combined-index bandwidth increases from 120.349 to 131.703 Hz. Peak reductions exceed 20 dB at several dominant modal frequencies, and 5% tuning scatter has only a small effect on the broadband averages.

Author contributions: Conceptualization, YN and MA; methodology, YN, MA, and SBM; software, YN and SBM; validation, MA, SIM, and AKS; formal analysis, YN and SBM; investigation, YN, MA, and AV; resources, AV, SIM, and AKS; data curation, SBM and AKS; writing—original draft preparation, YN; writing—review and editing, YN, AV, MA, SIM, and AKS; visualization, YN and SBM; supervision, AV and MA; project administration, YN and AV. All authors have read and agreed to the published version of the manuscript.

Funding: This research is funded by INTI International University, for APC charges only.

Institutional review board statement: Not applicable.

Institutional review board statement: Not applicable.

Informed consent statement: Not applicable.

Data availability statement: All data that are incorporated in the manuscript itself.

Conflict of interest: The authors declare no conflict of interest for this study.

AI use statement: The authors declare that no artificial intelligence (AI) tools were used in the preparation of this manuscript.

References

1. Smith MC. Synthesis of mechanical networks: The inerter. IEEE Transactions on Automatic Control. 2002; 47(10): 1648–1662. doi: 10.1109/TAC.2002.803532
2. Chen M, Papageorgiou C, Scheibe F, et al. The missing mechanical circuit element. IEEE Circuits and Systems Magazine. 2009; 9(1): 10–26. doi: 10.1109/MCAS.2008.931738
3. Liu C, Chen L, Lee HP, et al. A review of the inerter and inerter-based vibration isolation: Theory, devices, and applications. Journal of the Franklin Institute. 2022; 359(14): 7677–7707. doi: 10.1016/j.jfranklin.2022.07.030
4. Krenk S. Resonant inerter based vibration absorbers on flexible structures. Journal of the Franklin Institute. 2019; 356(14): 7704–7730. doi: 10.1016/j.jfranklin.2018.11.038
5. Taflanidis AA, Giaralis A, Patsialis D. Multi-objective optimal design of inerter-based vibration absorbers for earthquake protection of multi-storey building structures. Journal of the Franklin Institute. 2019; 356(14): 7754–7784. doi: 10.1016/j.jfranklin.2019.02.022
6. Su N, Bian J, Peng S, et al. Analytical optimal design of inerter-based vibration absorbers with negative stiffness balancing static amplification and dynamic reduction effects. Mechanical Systems and Signal Processing. 2023; 192: 110235. doi: 10.1016/j.ymssp.2023.110235
7. Xiao Y, Wen J, Wen X. Flexural wave band gaps in locally resonant thin plates with periodically attached spring–mass resonators. Journal of Physics D: Applied Physics. 2012; 45(19): 195401. doi: 10.1088/0022-3727/45/19/195401
8. Peng H, Frank Pai P. Acoustic metamaterial plates for elastic wave absorption and structural vibration suppression. International Journal of Mechanical Sciences. 2014; 89: 350–361. doi: 10.1016/j.ijmecsci.2014.09.018
9. Qin Q, Sheng MP. Analyses of multi-bandgap property of a locally resonant plate composed of periodic resonant subsystems. International Journal of Modern Physics B. 2018; 32(24): 1850269. doi: 10.1142/S0217979218502697
10. Li X, Wang Q. Analysis of the inherent instability of the interpolating moving least squares method when using improper polynomial bases. Engineering Analysis with Boundary Elements. 2016; 73: 21–34. doi: 10.1016/j.enganabound.2016.08.012
11. Andral U, Kibler B, Dudley JM, et al. Akhmediev breather signatures from dispersive propagation of a periodically phase-modulated continuous wave. Wave Motion. 2020; 95: 102545. doi: 10.1016/j.wavemoti.2020.102545
12. He ZC, Xiao X, Li E. Design for structural vibration suppression in laminate acoustic metamaterials. Composites Part B: Engineering. 2017; 131: 237–252. doi: 10.1016/j.compositesb.2017.07.076
13. Pai PF, Peng H, Jiang S. Acoustic metamaterial beams based on multi-frequency vibration absorbers. International Journal of Mechanical Sciences. 2014; 79: 195–205. doi: 10.1016/j.ijmecsci.2013.12.013
14. Hussein MI, Leamy MJ, Ruzzene M. Dynamics of Phononic Materials and Structures: Historical Origins, Recent Progress, and Future Outlook. Applied Mechanics Reviews. 2014; 66(4): 040802. doi: 10.1115/1.4026911
15. Liu Z, Zhang X, Mao Y, et al. Locally Resonant Sonic Materials. Science. 2000; 289(5485): 1734–1736. doi: 10.1126/science.289.5485.1734
16. Deymier PA. Acoustic Metamaterials and Phononic Crystals, Springer Series in Solid-State Sciences. Springer; 2013. doi: 10.1007/978-3-642-31232-8
17. Sugino C, Xia Y, Leadenham S, et al. A general theory for bandgap estimation in locally resonant metastructures.

Journal of Sound and Vibration. 2017; 406: 104–123. doi: 10.1016/j.jsv.2017.06.004

18. Wang G, Wen J, Wen X. Quasi-one-dimensional phononic crystals studied using the improved lumped-mass method: Application to locally resonant beams with flexural wave band gap. Physical Review B. 2005; 71(10): 104302. doi: 10.1103/PhysRevB.71.104302
19. Yu D, Liu Y, Wang G, et al. Flexural vibration band gaps in Timoshenko beams with locally resonant structures. Journal of Applied Physics. 2006; 100(12): 124901. doi: 10.1063/1.2400803
20. Krushynska AO, Miniaci M, Bosia F, et al. Coupling local resonance with Bragg band gaps in single-phase mechanical metamaterials. Extreme Mechanics Letters. 2017; 12: 30–36. doi: 10.1016/j.eml.2016.10.004
21. Wang P, Casadei F, Kang SH, et al. Locally resonant band gaps in periodic beam lattices by tuning connectivity. Physical Review B. 2015; 91(2): 020103. doi: 10.1103/PhysRevB.91.020103
22. Ma R, Bi K, Hao H. Inerter-based structural vibration control: A state-of-the-art review. Engineering Structures. 2021; 243: 112655. doi: 10.1016/j.engstruct.2021.112655
23. Brzeski P, Kapitaniak T, Perlikowski P. Novel type of tuned mass damper with inerter which enables changes of inertance. Journal of Sound and Vibration. 2015; 349: 56–66. doi: 10.1016/j.jsv.2015.03.035
24. Marian L, Giaralis A. Optimal design of a novel tuned mass-damper–inerter (TMDI) passive vibration control configuration for stochastically support-excited structural systems. Probabilistic Engineering Mechanics. 2014; 38: 156–164. doi: 10.1016/j.probengmech.2014.03.007
25. Lazar IF, Neild SA, Wagg DJ. Using an inerter-based device for structural vibration suppression. Earthquake Engineering & Structural Dynamics. 2014; 43(8): 1129–1147. doi: 10.1002/eqe.2390
26. Jain S, Tiso P. Model order reduction for temperature-dependent nonlinear mechanical systems: A multiple scales approach. Journal of Sound and Vibration. 2020; 465: 115022. doi: 10.1016/j.jsv.2019.115022
27. Zhou H, Li P, Fang Y. Thermoelastic damping in circular cross-section micro/nanobeam resonators with single-phase-lag time. International Journal of Mechanical Sciences. 2018; 142–143: 583–594. doi: 10.1016/j.ijmecsci.2018.05.024
28. Goldsberry BM, Haberman MR. Negative stiffness honeycombs as tunable elastic metamaterials. Journal of Applied Physics. 2018; 123(9): 091711. doi: 10.1063/1.5011400
29. Bacigalupo A, Gnecco G, Lepidi M, et al. Optimal design of low-frequency band gaps in anti-tetrachiral lattice meta-materials. Composites Part B: Engineering. 2017; 115: 341–359. doi: 10.1016/j.compositesb.2016.09.062
30. Baravelli E, Ruzzene M. Internally resonating lattices for bandgap generation and low-frequency vibration control. Journal of Sound and Vibration. 2013; 332(25): 6562–6579. doi: 10.1016/j.jsv.2013.08.014
31. Du Y, Zou T, Pang F, et al. Design method for distributed dynamic vibration absorbers of stiffened plate under different boundary constraints. Thin-Walled Structures. 2023; 185: 110494. doi: 10.1016/j.tws.2022.110494
32. Li L, Li B, Xu Z. Design of distributed dynamic absorbers for vibration suppression of panel structures. Acta Mechanica Sinica. 2024; 40(7): 523521. doi: 10.1007/s10409-023-23521-x
33. Zhang H, Chen MZQ. Analytical optimization of an inerter-based dynamic vibration absorber for suppressing plate vibration. IET Control Theory & Applications. 2024; 18(12): 1559–1568. doi: 10.1049/cth2.12702
34. Høgsberg J, Lossouarn B, Deü JF. Tuning of vibration absorbers by an effective modal coupling factor. International Journal of Mechanical Sciences. 2024; 268: 109009. doi: 10.1016/j.ijmecsci.2024.109009
35. Jamil F, Chen F, Deng B, et al. Inerter-based elastic metamaterials for band gap at extremely low frequency. Extreme Mechanics Letters. 2022; 56: 101847. doi: 10.1016/j.eml.2022.101847
36. Ye L, Yang Y, Ma W, et al. Design, Optimization, and Experimental Validation of Dynamic Vibration Absorber for Vibration Suppression in Cantilevered Plate Structures. Vibration. 2025; 8(3): 40. doi: 10.3390/vibration8030040
37. Guo Z, Xie B, Sheng M, et al. Tunable Ultralow-Frequency Bandgaps Based on Locally Resonant Plate with Quasi-Zero-Stiffness Resonators. Applied Sciences. 2024; 14(4): 1467. doi: 10.3390/app14041467
38. Xu Y, Hao Y, Zhang W, et al. Band gaps and dynamics of locally resonant meta-plate with stiffness adjustable low frequency resonator. Journal of Vibration and Control. 2024; 30(23–24): 5274–5286. doi: 10.1177/10775463231220434
39. Qin Y, Tan JJ, Hornikx M. Application of multiple dynamic vibration absorbers in reducing low-frequency vibration of a floor-like lightweight joist structure: Comparison of experimental and computational results. Applied Acoustics. 2023; 211: 109437. doi: 10.1016/j.apacoust.2023.109437
40. Gong C, Fang X, Li H, et al. Broadband vibration reduction through combined linear-nonlinear oscillators in a meta-plate. Journal of Sound and Vibration. 2026; 626: 119614. doi: 10.1016/j.jsv.2025.119614